Science Advances
AAAS

Supplementary Materials for

Polymorphic display and texture integrated systems controlled by capillarity

Jonghyun Ha *et al.*

Corresponding author: Sameh Tawfick, tawfick@illinois.edu

Sci. Adv. **9**, eadh1321 (2023)
DOI: 10.1126/sciadv.adh1321

The PDF file includes:

Supplementary Materials and Methods
Sections S1 to S9
Figs. S1 to S12
Tables S1 and S2
Legends for movies S1 to S7
References

Other Supplementary Material for this manuscript includes the following:

Movies S1 to S7

Supplementary Text

S1. Stability and persistence of fin morphing states

We test the persistence of texture states, both in the N-mode and W-mode. Figure S2 shows the results of the persistence duration in each state. We observed that flap4 maintain its state for at least 3 days due to the small mineral oil meniscus formed at the interface between the fin and the device walls. This is aided by the use of an almost nonevaporating liquid (e.g., mineral oil), so the surface tension can permanently hold the flapped fins. Here, the capillary force acting on the fins can be written as γb, where γ is the surface tension and b is fin width. The elastic resisting force depending on a deflection, δ, can be written as $EI/l^3\delta$, where E, I, and l are the Young's modulus, second moment of area of fins, and fin length respectively. For δ, we use W (wide spacing) being higher than N (narrow spacing), so $\delta = W$. When $b = 5$ mm, $l = 6$ mm, and $W = 4$ mm (typical values in the experiments), capillary and elastic restoring forces are orders of 0.1 and 0.01 mN, respectively. Therefore, the persistence in both states is due to the capillary forces being one order of magnitude higher than the elastic restoring force.

S2. Experimental studies of texture morphing behavior in relation to the N and W ratio

We experimentally investigate the fin bending direction depending on the portion of the narrow and wide sides. We set the design parameters such that the capillary pressure on the left side (γ/N) is stronger than that on the right side (γ/W), i.e., $N < W$, and fix the width of the wide side, W, to 4 mm. We then vary the total cell size $N+W$ from 5.5 mm to 7 mm by changing N from 1.5 mm to 4 mm. Here, we note that the portion between N and W plays an important role in texture morphing, rather than the overall cell size ($N+W$). Our parametric analysis reveals that the drain flow rates for the W-mode increase as the portion of the wide side, $W/(N+W)$, increases. As shown in Fig. 1D, the transition flow rate is approximately 10 ml/min when $W/(N+W) = 4/5.5$ (blue colors), whereas it is 1 ml/min when $W/(N+W) = 4/7$ (pink colors). Conversely, this trend is reversed when we consider the portion of the narrow side, $N/(N+W)$. Therefore, we conclude that the ratio of the wide and narrow sides plays a significant role in the texture morphing trend.

The fin length, l, is inherently affected by $N+W$ since the fin must cover the overall cell when it deforms. This allows us to predict the transition between W-mode and N-mode regarding to the flow rates, even though we did not experimentally vary the total cell size $N+W$ with the same portion of the narrow and wide sides. As the cell size increases, leading to an increment of l, we require faster drain rates or a large capillary number (Ca) to obtain W-mode according to Fig. 1F.

S3. Effects of liquid viscosity

While in most experiments we used a light mineral oil (viscosity ~ 0.02 Pa.s), we also tested the use of heavy viscous liquid to investigate how the liquid viscosity influences the texture morphing Table S1). With high viscosity liquids (~ 0.15 Pa.s), the transition drain rate between N-mode and W-mode decreases, as shown in Fig. S3A. This lower transition point is mainly due to the resistance to liquid shearing through the small spacing s (increment of μ). Using our model, we still show the model agrees well with the different experimental result, as shown in Fig. S3B.

S4. Limits of fin stiffness and operation in the symmetric far-walls limit

In addition to testing the flap4 devices having asymmetric spacings between the fin and walls (*N* and *W*), we studied the behavior of fins in the symmetric far-walls limit. In this case, a single fin is submerged in a cell, where the liquid is drained from both sides simultaneously, the walls forming the channel widths are very far and do not affect the fin (much larger than the meniscus). The study shows two modes: piercing and collapsing, depending on the stiffness of the fin. The study shows no dependance on the drain dynamics. Also, as expected, in the collapse mode, the fins bend and buckle to either the left or right side with equal probabilities. When the fin stiffness is high, it pierces the liquid interface without deformation. Figure S4A shows the schematics of the piercing and collapsing modes. Based on the elastocapillary number (*13, 14*), $\eta = l/l_{ec}$, we theoretically predict the transition region between the piercing and collapsing, as shown in Fig. S4B. When $\eta > 0.8$, the fin always collapses regardless of the drain dynamics, while we consistently observe the piercing mode when $\eta < 0.8$. According to Fig. S4B, we note that the deformation mode in the symmetric far-walls limit is independent of the drain rates. This is in contrast with the devices in Fig. 1 showing a clear drain rate u dependence.

S5. Reduced-order modeling

We constructed a reduced-order model to study the dynamic fluid-structure behavior associated with the flapping of the single fin flap-phore. Specifically, we consider a 2D hydrodynamic lubrication fluid model assuming that the flow velocity along the width d can be ignored. This simplification enables a simple reduced-order model that can be solved numerically in a straight-forward manner and provide useful insights. We note that the Bond number $\rho g l^2/\sigma \sim 1$, where ρ is the density and σ is the surface tension of the liquid, indicating the need to consider hydrostatic pressure. On the other hand, the inertial effects of the liquid and the fin are neglected due to the extremely small Reynolds number $\rho u l/\mu \sim 0.1$. In addition, a pseudo-rigid-body model is used where the elastic fin is treated as a rigid body attached to the substrate via a torsional spring of spring constant K_θ. N and W are the fixed side length at the base of the narrow and wide chambers, respectively. The liquid has a viscosity μ. The liquid drains out from the W-side of the system at a constant rate $Q_W > 0$. Also, the internal flow rate between chambers is defined as Q_N, where $Q_N > 0$ means the liquid is flowing from the narrow to the wide chamber.

We define three dynamic variables in this reduced order model, h_N and h_W the liquid height in the narrow and wide chambers, respectively, and θ the fin inclination angle with respect to its initial vertical position. Since the leakage between the two chambers takes place within the spacing s in the three-dimensional real system, which lies outside the planar representation of the device, the two-dimensional reduced order model uses a leakage channel to connect the two chambers, as shown in Fig. S5. In the real system, the leakage flow cross section is $\sim ls$, and the length of the leakage flow path is equal to the fin thickness b, where the flow is constricted between the fin and the wall in the out of plane direction. Since the flap-phores are designed to have the fin length almost equal to the width, i.e. $l \sim d$, we can consider in the reduced-order model a channel of thickness s and leakage flow path length b in the 2D model. The hydrodynamics of flow Q_N and fluid shear only develop within this region sb in the reduced-order model. In Fig. S5, the hatched blue region is created to visualize the continuity of flow in the reduced-order model, and hence the hydrodynamics of flow in the hatched area is not modeled, as it does not exist in the real system. Moreover, in the real system, the shear forces which develop in the leakage region s act on the fin and cause its deflection. Accordingly, in the reduced order model, the fluid shear is transferred from the leakage channel to the center point of the fin, so we refer to the leakage region as the "fin avatar" because it transfers the fluid shear forces from the leakage channel to a torque on the fin. Considering the full model, three differential equations are used to solve for the three dynamic variables: conservation of mass, pressure equation, and torque equation.

The experiments show the importance of the contact angle evolution when the liquid is pinned at the top corner of the fins. More precisely, the fin can be stabilized in the vertical position due to the pinning, and we observe that when the liquid is not pinned at the corner (e.g. by using a much longer fin height), the fin does not have a static equilibrium. We model the liquid pinning to the fins corner which induces a transient evolution of the contact angles in response to the applied flow Q_W. The liquid surface in both chambers is initially at the same height as the tip of the fin, that is, $h_N(t=0) = h_W(t=0) = l$, with initial contact angles $\alpha_N(t=0) = \alpha_W(t=0) = 90^\circ$. This initial condition is selected to stabilize the fin rotation at the onset of simulation, which agrees with the experiments. The instantaneous contact angle is governed by the relative position between the liquid height and the tip of the fin where triple line pinning occurs, and is written as

$$\begin{aligned} l\cos\theta - h_N &= \tfrac{1}{2}(N + \theta h_N)\left(\tfrac{1}{\cos\alpha_N} - \tan\alpha_N\right) \\ l\cos\theta - h_W &= \tfrac{1}{2}(W - \theta h_W)\left(\tfrac{1}{\cos\alpha_W} - \tan\alpha_W\right) \end{aligned} \qquad \text{(S1)}$$

where α_N and α_W are the contact angles between liquid and wall in the narrow and wide chamber, respectively. As the liquid descends, the meniscus builds up. Consequently, the contact angle decreases until the meniscus fully develops ($\alpha = 23^\circ$) and meets the solid fin at its flat surface.

5.1. Conservation of mass

Using the small angle approximation, we obtain the 2D leakage flow rate $-Q_N/d$ and $(Q_N - Q_W)/d$ as a function of independent variables h_N, h_W, θ, and their derivatives with respect to time.

$$\begin{aligned} -\tfrac{Q_N}{d} &= \dot{h}_N(N + \theta h_N) + \tfrac{1}{2}\dot{\theta} h_N^2 \\ \tfrac{Q_N - Q_W}{d} &= \dot{h}_W(W - \theta h_W) - \tfrac{1}{2}\dot{\theta} h_W^2. \end{aligned} \qquad \text{(S2)}$$

Combining the net flow rate of each chamber in Eq. S2, the liquid drain rate from the pump satisfies

$$\tfrac{Q_W}{d} = -\left[\dot{\theta}\tfrac{1}{2}(h_N^2 - h_W^2) + \dot{h}_N(N + \theta h_N) + \dot{h}_W(W - \theta h_W)\right]. \qquad \text{(S3)}$$

5.2. Pressure equation

The flow in each chamber is driven by the suction pressure of the pump, the motion of the fin, and gravity. In other words, these effects generate a pressure gradient in the vertical direction of each chamber, and that pressure difference drives the flow. We first write the Generalized Reynold Equation which describes the pressure difference along each flow chamber $P(y,t)$

$$\tfrac{\partial P}{\partial y} = -\tfrac{12\mu}{j(y,t)^3}\tfrac{Q}{d} - \rho g, \qquad \text{(S4)}$$

where $j(y,t)$ is the flow chamber width, which depends on the height due to the fin's inclination, and Q/d is the 2D flow rate along the vertical direction. From the conservation of mass, we derive the relation between the side distance $j(y,t)$ and flow rate Q/d as $-\frac{\partial j(y,t)}{\partial t} = \frac{\partial}{\partial y}\frac{Q}{d}$.
Applying the lubrication theory, we can write the governing equation of the flow as

$$\frac{j(y,t)^3}{12\mu}\frac{\partial^2 P}{\partial y^2} = \frac{\partial j(y,t)}{\partial t}. \tag{S5}$$

The first boundary condition is the Laplace pressure. Since the liquid meniscus is formed at $y = h$, the Laplace equation governs the pressure right below the liquid surface

$$P|_{y=h} = -\frac{2\sigma\cos\alpha}{j(y=h,t)}, \tag{S6}$$

where α is the liquid-wall meniscus contact angle.
The second boundary condition is for the derivative of the pressure with respect to the coordinate y at the bottom of the chamber $\frac{\partial P}{\partial y}|_{y=0}$. While in the real system the leakage flow takes place along the length of the fins, in the reduced order model, we assume that the leakage flow is at the bottom of the container, and that the pump applies a constant flow rate to the bottom of the wide chamber. This leads to the boundary condition at the bottom of each chamber

$$\frac{\partial P}{\partial y}|_{y=0} = -\frac{12\mu}{j(y=\frac{h}{2},t)^3}\frac{Q}{d} - \rho g. \tag{S7}$$

where we use the average chamber width $j(y=\frac{h}{2},t)$.

Now, we can solve the pressure profile of each chamber by integrating equation (5) with the boundary conditions (6) and (7). For the narrow chamber, we have $j(y,t) = j_N = N + \theta y$ and $h = h_N$. Thus, the pressure at the bottom of the narrow chamber yields

$$P_N|_{y=0} = -\frac{2\sigma\cos\alpha_N}{N+\theta h_N} + \rho g h_N + 6\mu\dot{\theta}\left[\frac{3+2\ln N}{2\theta^3} + \frac{h_N^3}{\left(N+\frac{1}{2}\theta h_N\right)^3} - \frac{N(4\theta h_N+3N)}{2\theta^3(\theta h_N+N)^2} - \frac{\ln(\theta h_N+N)}{\theta^3}\right] + \frac{12\mu h_N}{\left(N+\frac{1}{2}\theta h_N\right)^3}(N+\theta h_N)\dot{h}_N. \tag{S8}$$

Similarly, for the wide chamber, $j(y,t) = j_W = W - \theta y$ and $h = h_W$, so we obtain the pressure at the bottom of the wide chamber

$$P_W|_{y=0} = -\frac{2\sigma\cos\alpha_W}{W-\theta h_W} + \rho g h_W + 6\mu\dot{\theta}\left[\frac{W(4\theta h_W-3W)}{2\theta^3(W-\theta h_W)^2} - \frac{\ln(W-\theta h_W)}{\theta^3} - \frac{-3-2\ln W}{2\theta^3} - \frac{h_W^3}{\left(W-\frac{1}{2}\theta h_W\right)^3}\right] + \frac{12\mu h_W}{\left(W-\frac{1}{2}\theta h_W\right)^3}(W-\theta h_W)\dot{h}_W. \tag{S9}$$

The lubrication approximation is also applied within the leakage between two chambers. Since, in the real system, the leakage flow between the narrow and the wide chamber is through the two out-plane spacings s between the fins and the walls, in the reduced-order model the 2D flow rate within the channel is equal to $q = Q_N/h_N$.

Consequently, the average pressure difference across the gap is dominated by the flow q and the fin average translational velocity $V = \frac{1}{2}h_N\dot{\theta}$, which can be expressed as

$$\Delta P_{across} = P_W|_{y=0} - P_N|_{y=0} = 2\left(-\frac{6\mu}{s^3}qb + V\frac{6\mu}{s^2}b\right), \tag{S10}$$

where b is the thickness of the fin and the second term on the right-hand side is the Couette flow within the leakage channel where the fin avatar moves horizontally at a velocity V.

In conclusion, combining Eq. S8, S9, and S10, we obtain the pressure balance equation

$$\dot{\theta}6\mu\left(\frac{\ln\frac{N}{W}+\ln\left(\frac{W-\theta h_W}{\theta h_N+N}\right)}{\theta^3}+\frac{h_N^3}{\left(N+\frac{1}{2}\theta h_N\right)^3}-\frac{N(4\theta h_N+3N)}{2\theta^3(\theta h_N+N)^2}+\frac{h_W^3}{\left(W-\frac{1}{2}\theta h_W\right)^3}-\frac{W(4\theta h_W-3W)}{2\theta^3(W-\theta h_W)^2}+\frac{h_N}{s^2}b+\frac{dbh_N}{s^3}\right)+\dot{h}_N\left(\frac{12\mu h_N(N+\theta h_N)}{\left(N+\frac{1}{2}\theta h_N\right)^3}+\frac{12\mu db(N+\theta h_N)}{s^3 h_N}\right)-\dot{h}_W\frac{12\mu h_W(W-\theta h_W)}{\left(W-\frac{1}{2}\theta h_W\right)^3}=\rho g(h_W-h_N)+\frac{2\sigma\cos\alpha_N}{N+\theta h_N}-\frac{2\sigma\cos\alpha_W}{W-\theta h_W}. \quad \text{(S11)}$$

5.3. Torque equation

Balancing the torques is used to derive the conservation of momentum. Fig. S6 is the free body diagram showing all torques acting on the fin. Neglecting the small inertia term of the fin, the pressure torque on the fin T_P should balance with the torque due to shear force on the fin side T_τ, the torque due to horizontal component of the surface tension T_σ, and the restoring torque due to fin elasticity T_θ as

$$\sum T = T_P + T_\tau + T_\sigma + T_\theta = 0. \quad \text{(S12)}$$

From the lubrication Eq. S5 with boundary conditions, Eq. S6 and S7, we derive the torque due to the pressure normal to the fin surface as

$$T_P = d\int_0^{h_N} P_N\cdot y\,\mathrm{d}y - d\int_0^{h_W} P_W\cdot y\,\mathrm{d}y. \quad \text{(S13)}$$

Next, from Eq. S10, the pressure difference across the gap generates a shear load on the effective fin. The rigid connection between the effective fin and the actual fin transfers a resultant shear torque T_τ to the actual fin, which can be expressed as

$$T_\tau = 2\mu\left(\frac{4}{s}V-\frac{3}{s^2}q\right)\frac{1}{2}h_N^2 b. \quad \text{(S14)}$$

Moreover, the expression of the capillary torque due to the surface tension at the meniscus is $T_\sigma = -\sigma d h_N\sin\alpha_N + \sigma d h_W \sin\alpha_W$. Combining all toques with the resisting torque due to fin elasticity $T_\theta = -K_\theta\theta$ and normalizing with the fin width d, we write the final balance of torque Eq. S12:

$$\dot{\theta}\mu\left[\frac{3(-h_N^2+h_W^2)}{2\theta^3}+\frac{15(Nh_N+Wh_W)}{\theta^4}+\frac{3(N^2-W^2)+18N^2\ln\frac{N}{N+h_N\theta}-18W^2\ln\frac{W}{W-h_W\theta}}{\theta^5}-\frac{9N^2h_N^2+12N\theta h_N^3}{2N^2\theta^3+4Nh_N\theta^4+2h_N^2\theta^5}-\frac{-9W^2h_W^2+12W\theta h_W^3}{2W^2\theta^3-4Wh_W\theta^4+2h_W^2\theta^5}-\frac{3N^3}{N\theta^5+h_N\theta^6}-\frac{3W^3}{-W\theta^5+h_W\theta^6}+\frac{h_N^5}{\left(N+\frac{1}{2}\theta h_N\right)^3}+\frac{h_W^5}{\left(W-\frac{1}{2}\theta h_W\right)^3}-\left(\frac{2h_N^3 b}{sd}+\frac{3h_N^3 b}{2s^2}\right)\right]+\dot{h}_N\mu(N+\theta h_N)\left(\frac{2h_N^3}{\left(N+\frac{1}{2}\theta h_N\right)^3}-\frac{3bh_N}{s^2}\right)-\dot{h}_W\mu(W-\theta h_W)\left(\frac{2h_W^3}{\left(W-\frac{1}{2}\theta h_W\right)^3}\right)=\frac{K_\theta\theta}{d}+\sigma h_N\sin\alpha_N-\sigma h_W\sin\alpha_W-\left(-\frac{\sigma\cos\alpha_N}{N+h_N\theta}+\frac{\rho g h_N}{6}\right)h_N^2+\left(-\frac{\sigma\cos\alpha_W}{W-h_W\theta}+\frac{\rho g h_W}{6}\right)h_W^2. \quad \text{(S15)}$$

Finally, we may combine Eq. S3, S11, and S15 to conclude a matrix of system reduced order ODEs

$$\begin{bmatrix} \frac{1}{2}(h_W^2-h_N^2) & -(N+\theta h_N) & -(W-\theta h_W) \\ Term\ 1^* & \left(\frac{12\mu h_N(N+\theta h_N)}{\left(N+\frac{1}{2}\theta h_N\right)^3}+\frac{12\mu db(N+\theta h_N)}{s^3 h_N}\right) & -\frac{12\mu h_W(W-\theta h_W)}{\left(W-\frac{1}{2}\theta h_W\right)^3} \\ Term\ 2^* & \mu(N+\theta h_N)\left(\frac{2h_N^3}{\left(N+\frac{1}{2}\theta h_N\right)^3}-\frac{3bh_N}{s^2}\right) & -\mu(W-\theta h_W)\left(\frac{2h_W^3}{\left(W-\frac{1}{2}\theta h_W\right)^3}\right) \end{bmatrix} \times \begin{bmatrix} \dot{\boldsymbol{\theta}} \\ \dot{h}_N \\ \dot{h}_W \end{bmatrix} =$$

$$\begin{bmatrix} \frac{Q_W}{d} \\ \rho g(h_W-h_N)+\frac{2\sigma\cos\alpha_N}{N+\theta h_N}-\frac{2\sigma\cos\alpha_W}{W-\theta h_W} \\ \frac{K_\theta \theta}{d}+\sigma h_N \sin\alpha_N-\sigma h_W\sin\alpha_W-\left(-\frac{\sigma\cos\alpha_N}{N+h_N\theta}+\frac{\rho g h_N}{6}\right)h_N^2+\left(-\frac{\sigma\cos\alpha_W}{W-h_W\theta}+\frac{\rho g h_W}{6}\right)h_W^2 \end{bmatrix}$$

$$Term\ 1: 6\mu\left(\frac{\ln\frac{N}{W}+\ln\left(\frac{W-\theta h_W}{\theta h_N+N}\right)}{\theta^3}+\frac{h_N^3}{\left(N+\frac{1}{2}\theta h_N\right)^3}-\frac{N(4\theta h_N+3N)}{2\theta^3(\theta h_N+N)^2}+\frac{h_W^3}{\left(W-\frac{1}{2}\theta h_W\right)^3}-\frac{W(4\theta h_W-3W)}{2\theta^3(W-\theta h_W)^2}+\frac{h_N}{s^2}b+\frac{dbh_N}{s^3}\right); \tag{S16}$$

$$Term\ 2: \mu\left[\frac{3(-h_N^2+h_W^2)}{2\theta^3}+\frac{15(Nh_N+Wh_W)}{\theta^4}+\frac{3(N^2-W^2)+18N^2\ln\frac{N}{N+h_N\theta}-18W^2\ln\frac{W}{W-h_W\theta}}{\theta^5}-\frac{9N^2h_N^2+12N\theta h_N^3}{2N^2\theta^3+4Nh_N\theta^4+2h_N^2\theta^5}-\frac{-9W^2h_W^2+12W\theta h_W^3}{2W^2\theta^3-4Wh_W\theta^4+2h_W^2\theta^5}-\frac{3N^3}{N\theta^5+h_N\theta^6}-\frac{3W^3}{-W\theta^5+h_W\theta^6}+\frac{h_N^5}{\left(N+\frac{1}{2}\theta h_N\right)^3}+\frac{h_W^5}{\left(W-\frac{1}{2}\theta h_W\right)^3}-\left(\frac{2h_N^3 b}{sd}+\frac{3h_N^3 b}{2s^2}\right)\right].$$

The numerical computation of pressure and torque shows that the matrix equations will have an integration issue when $|\theta| < 0.5^\circ$. We also note that *Term 1* and *Term 2* in Eq. S16 reach a numerical singularity at $\theta = 0$, where the system is at the initial equilibrium. To solve the equations at small rotation angles, we solve Eq S5 and the boundary conditions, Eq. S6 and S7 with the approximations $j_N \approx N, \frac{\partial j_N}{\partial t} = \dot{\theta}y,$ and $j_W \approx W,\ \frac{\partial j_W}{\partial t} = -\dot{\theta}y$. This leads to the system ODE matrix at $-0.5^\circ < \theta < 0.5^\circ$

$$\begin{bmatrix} \frac{1}{2}(h_W^2-h_N^2) & -(N+\theta h_N) & -(W-\theta h_W) \\ \frac{4\mu h_N^3}{N^3}+\frac{4\mu h_W^3}{W^3}+\frac{6\mu h_N b}{s^2}+\frac{6\mu dbh_N}{s^3} & \left(\frac{12\mu h_N}{N^2}+\frac{12\mu dbN}{s^3 h_N}\right) & -\frac{12\mu h_W}{W^2} \\ \frac{2\mu h_N^5}{5N^3}+\frac{2\mu h_W^5}{5W^3}-\left(\frac{2\mu h_N^3 b}{sd}+\frac{3\mu h_N^3 b}{2s^2}\right) & \frac{2\mu h_N^3}{N^2}-\frac{3N\mu bh_N}{s^2} & -\frac{2\mu h_W^3}{W^2} \end{bmatrix} \times \begin{bmatrix} \dot{\theta} \\ \dot{h}_N \\ \dot{h}_W \end{bmatrix} = \begin{bmatrix} \frac{Q_W}{d} \\ \rho g(h_W-h_N)+\frac{2\sigma\cos\alpha_N}{N}-\frac{2\sigma\cos\alpha_W}{W} \\ \frac{K_\theta\theta}{d}+\sigma h_N\sin\alpha_N-\sigma h_W\sin\alpha_W-\left(-\frac{\sigma\cos\alpha_N}{N}+\frac{\rho g h_N}{6}\right)h_N^2+\left(-\frac{\sigma\cos\alpha_W}{W}+\frac{\rho g h_W}{6}\right)h_W^2 \end{bmatrix}. \tag{S17}$$

The combination of Eq. S1, S16, and S17 presents the complete formulation of the system numerical simulation for both small (Eq. S17) and large (Eq. S1 and S6) rotation angles.

S6. Power consumption of flap4 and its comparison

We note that the resolution, refresh rate, and power requirements of the flap4 sizes in this study make them suitable for large displays used in civilian or military structures with responsive facades, vehicle body, or billboards. The power dissipation of the flap4 devices takes place in three sub-systems:

a. Viscous losses in the device and tubing
b. Viscous losses in the pump used to drive the flow
c. Electronic losses in the drive system (suggested by the reviewer)

First, we analyze the losses in (a) as shown in the new Fig. S8 by incorporating the tubing connected to the flap4, which necessitates additional energy to counteract the viscous resistance. There are two typical sources of viscous energy consumption for the operation of flap4: the pressure difference within the tubing Δp_t and within the flap4 Δp_s. By employing Poiseuille's equation, Δp_t is determined as $\Delta p_t \sim \mu Lq/R^4$, where L is the tubing length and R is the tubing radius equal to 0.8 mm (see Fig. S8). To obtain the W-mode, the used flow rate is q = 9.1 ml/min (see Fig. 1B), and the pressure difference $\Delta p_t \sim 10^3$ Pa. Consequently, the power consumption to generate the liquid flow in the tubing alone is approximated as $P_t \sim q\Delta p_t \sim 10^{-1}$ mW if the L = 100 mm and $P_t \sim 10^{-2}$ mW if L = 10 mm, the latter would be a practically reasonable length. Within the flap4 device, the hydrodynamic suction pressure generated within the narrow gap, s, can be expressed as: $\Delta p_s \sim \mu q/(ls^2)$. For the given experimental parameters (μ = 0.02 Pa·s, l = 6 mm, s = 0.4 mm, q = 9.1 ml/min), the calculated Δp_s is approximately 10^0 Pa, so $P_s \sim q\Delta p_s \sim 10^{-4}$ mW. Comparing the two pressure differences, Δp_s and Δp_t, it is evident that Δp_t is significantly larger than Δp_s ($\Delta p_t >> \Delta p_s$). This suggests that the theoretical power of the devices is indeed very small, even when the tubing is considered. By selecting, for instance, a larger tube diameter, the power consumed in the tubing will further drop until it becomes on the same order of the device itself. Next, we examine the implications of power consumption factoring in the display's refresh rate.

Flap4 is a reflective display panel like E-paper, unlike an emissive display. Therefore, it is more suitable to compare it with E-paper, which has almost zero power consumption until the display signal is changed, similar to flap4. Both E-paper and flap4 require power when refreshing the display. The previous power consumption calculation for flap4 did not include the refresh rate, f, so we have revised the formulation to include this variable to enable a comparison with E-paper. The typical refresh rate for video operation is f = 30 Hz. The power density of E-paper is approximately 100 mW/cm^2, as indicated by previous studies (*23*). We note that E-paper is usually appropriate for digital books rather than video operations, which is similar to flap4.

For flap4, we first set the pixel size λ for a cubic flap4 cell, as shown in Fig. S9A. Please note that the previous geometrical parameters (l, d, and N+W) are replaced with λ to simplify the calculation of the power per pixel. We consider a hydrodynamic time scale $\tau \sim \lambda^3/q$ as the refresh rate f =1/(2τ), where 2τ is corresponding to the one periodic motion for draining and filling (see Fig. S9B). Using the suction pressure of flap4, $\Delta p_s \sim \mu q/(\lambda s^2) \sim \mu\lambda^2/(s^2\tau)$, we obtain the power consumption $P \sim \Delta p_s q \sim \Delta p_s \lambda^3/\tau \sim \mu\lambda^5/(s\tau)^2$. μ, λ, and s are liquid viscosity, pixel (cell) size, and spacing, respectively. Therefore, the power density (power consumption per unit area λ^2) is $P^* \sim \mu\lambda^3/(s\tau)^2$. Replacing τ with 1/(2f), $P^* \approx \mu\lambda^3(2f)^2/s^2$. This simple scaling law leads to the power density of flap4 as function of refresh rate. For f = 30 Hz with the current design parameters (μ =

0.02 Pa·s, $s = 0.4$ mm, $\lambda \approx 7$ mm), $P^* \sim 10$ mW/cm^2 which is 10 times smaller than P^* of E-paper at the same rate.

Table S2 compares the specifications of conventional displays, providing a more comprehensive evaluation of flap4's performance in the context of existing technologies (*24*). Our results demonstrate that flap4 has a remarkable energy advantage compared to other display technologies. However, it is noteworthy that the current resolution (pixel size λ) of flap4 makes it suitable for large displays for applications like aircraft, automotive, or billboards. Flap4 devices are not suitable for hand-help devices, because of fabrication limitation. If new fabrication technology enables smaller pixels on the order of 0.5 mm, we anticipate that the power density will considerably decrease as $P^* \sim 10^{-2}$ mW/cm^2, as per the cube law in λ, once we successfully fabricate high-definition pixels with dimensions of $\lambda \approx 1$ mm. We note that the values in the Table, which are the typical values reported in the literate, ignore the power consumption in the electronic controllers.

The power contributions of operating the pump (b) and the electronic drivers (c) depend on the type of pump and electronic drive. First, pumping efficiency is described in the engineering practice by a metric known as overall efficiency where $\eta_{overall} = P_{out}^{mech}/P_{in}^{elect}$ i.e. it includes the electronic or electric drive power, the electric motor power, and the viscous dissipation within the body of the pump. Typical pump efficiencies range from 60-80% (*25*), where the electronic drives are optimized to use minimal power, and the motors are optimized to achieve >85% efficiency. This efficiency is achieved when the pump is precisely selected for the required mechanical work, and this is why pumps come is a variety of sizes. Importantly, the electric drive must be tailored to the motor, which is in turn tailored to the mechanical work. Otherwise, the efficiency significantly drops when general purpose electronic components are employed. An example of an inefficient pumping system is the lab syringe pump, where the efficiency is expected to be < 1% since the device is built for research where it can cover a very wide range of pressures and flow rates using a stepper motor (less efficient than DC motor) and drivers to provide a wide range of power and step frequency to the motor.

We attempted to use a general purpose micropump to operate the flap4 system. Commercial pumps are available for purchase in the market for microfluidic health care devices. The pump that we used is *Bartels, mp6-liq* with *mp-Highdriver*. This piezohydraulic pumps is suitable in terms of flow rate, but is designed for low viscosity fluids. We successfully used it to operate the device in the N- and W-modes using a low viscosity fluid (IPA), as shown in Fig. S10. According to the literature, the internal electrical to hydraulic efficiency of this pump is extremely high, approaching 99% (*26*). However, for this pump, the electronic drive supplied by the manufacturer is a general frequency controller, and hence also has an efficiency of < 1%, since the power efficiency is not a consideration for general purpose lab, instead the electronic board is designed to provide a wide range of operating conditions. Indeed, we performed a test to measure the efficiency of the electronic drive supplied by the pump manufacturer, mp-Highdriver, and found that it is efficiency is ~1%. This does not mean that a higher efficiency electronic driver is not possible, especially if another pump type is used.

In summary, we conclude that the overall power efficiency including the electronic control is important, and it should be the subject of future studies. It is evident from the data in the tables and references that flap4 will be much more power efficient that E-paper because the overall power efficiency of micropumps, optimized for a certain application, is expected to exceed 60% on a regular basis.

S7. Binary code

Using ASCII (American Standard Code for Information Interchange) code, we can exploit the soft reflective display composed of flap4s for applying to the binary coding system. Figure S11A illustrates the code description of ASCII in each alphabet. The same configuration with Fig. 4D can provide the binary encoded display, as described in Fig. S11B. In optical domain, the display encodes the word UIUC. In IR domain, it encodes the word UIUC.

S8. Feasibility test of flap4 on curved surfaces

We conduct an experimental study to investigate the stability of the capillary-driven morphing texture system on curved surfaces. We study 8 cases as shown in Fig. S12A:

- Flat devices curved to a convex configuration (2 different curvatures)
- Flat devices curved to a concave configuration (2 different curvatures)
- Curved devices having a convex geometry (fabricated with 2 different curvatures)
- Curved devices having a concave geometry (fabricated with 2 different curvatures)

We fabricate interconnected flap4s in three columns on two distinct surfaces with different curvatures, then capture the top view of the morphing behavior of flap4. Figure S12B shows the experimental setup of operation text of convex curvilinear surface. We observe that the operation is stable on a surface with a larger radius of curvature (R_1 = 100 mm) in all the cases tested, but unstable on a surface with a smaller radius of curvature (R_2 = 25 mm). This trend holds for both convex and concave, as well as for both bent-flat and fabricated curved surfaces. We use green (O) and orange (X) markings to denote operation stability, as shown in Fig. S12C. In particular, with a small-radius convex curvature, the fins tend to align perpendicularly to the circular arc, causing the left and right-side fins to initially bend outward (see the red arrows of the left-side orange box in Fig. S12C). This leads to N-mode and W-mode for the left-side and right-side fins, respectively, as shown in the small radius of convex shape of Fig. S12C. In the case of a small-radius concave curvature, we observe a buckling configuration, leading to cell collapse. These results suggest that the performance of the system may be influenced by the curvature of the surface, and more curved surfaces could potentially lead to unstable operation. Further research is necessary to examine the quantitative relationship between the system's performance and surface curvature in greater detail.

S9. Effects of gravity

The flap4 with their current size will operate stably up to moderate angles of <10°, like those demonstrated in the curved case with 1 mm radius of curvature. However, the operation will be influenced by the gravity effect, so the liquid in the flpa4 will spill out when the system flips over, or if tilted to larger angles. However, this behavior is fortunately size dependent. Theoretical prediction indicates that the sensitivity to gravity drops when the cell size is smaller than the capillary length, $l_c \sim [\gamma/(\rho g)]^{1/2}$, where the system will stably operate regardless of the gravity effect. According to theoretical analysis, stable operation in any orientation will be warranted for very thin fin structures on order of 10 µm with 1 mm height. Note that the gravity has almost no effect on the fins self-mass induced bending. Unfortunately, the resolution of our 3D printer used to produce the molds is around 50 µm, and the removal of fins from molds make the fabrication of molds for a gravity-agnostic flap4 extremely challenging to achieve within the scope of this study.

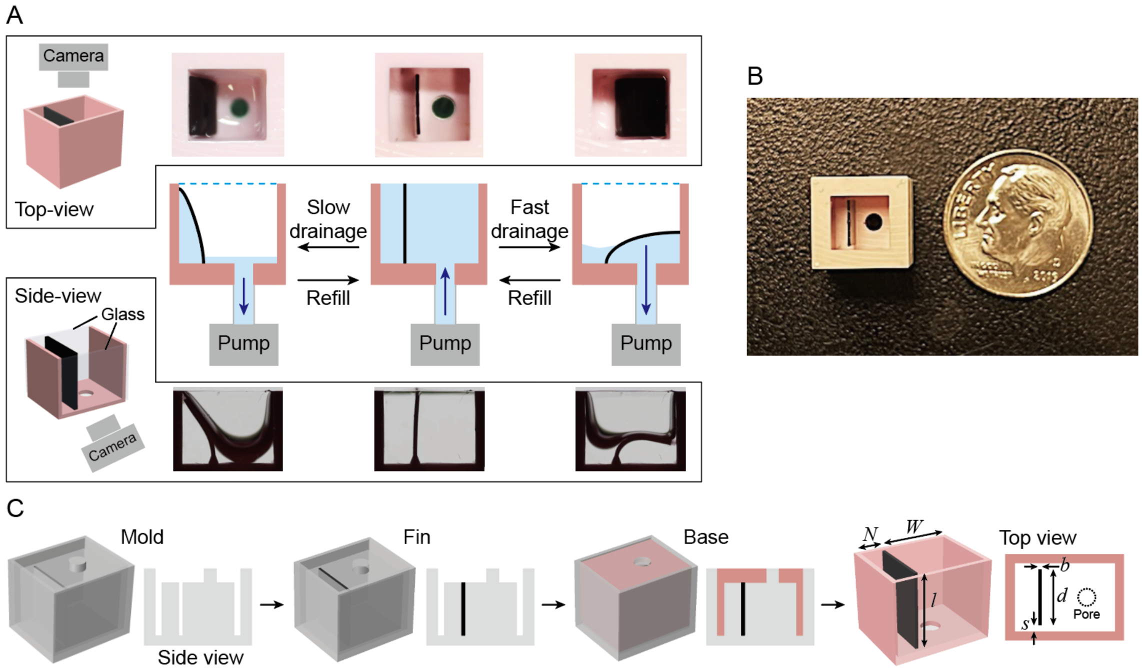

Fig. S1. Experimental setup description. (A) Optical images and schematics of the experimental methods. We attach the syringe pump to the bottom side of the device and drain/supply the liquid through the tubing. Two cameras are used to optically observe the fin texture from the top and side views. The fin width and length are 5 mm. **(B)** Size of the soft cell (flap4). We show the size of flap4 is smaller than a dime. **(C)** Fabrication method of soft texture-shifting system. We pour the silicon polymer (Elite Double 8, Zhermack) into the mold. The black and pink polymer have the same mechanical properties since the black pigment concentration is extremely low.

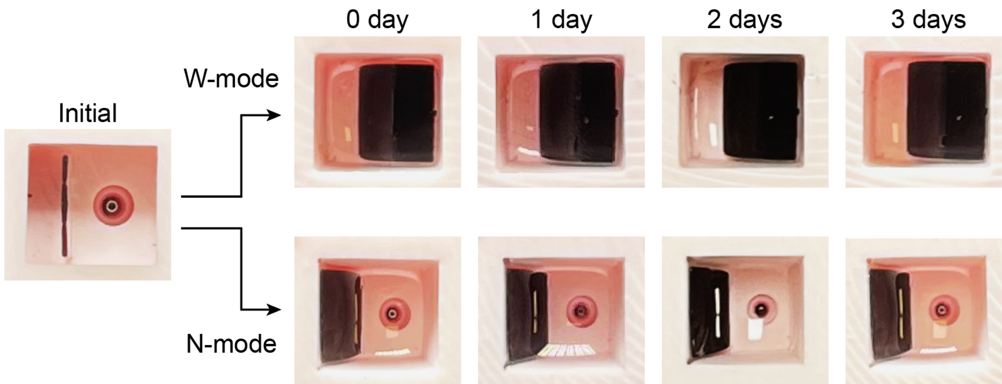

Fig. S2. State persistence test. Flap4s keep their textures in N-mode and W-mode up to at least three days when using the mineral oil.

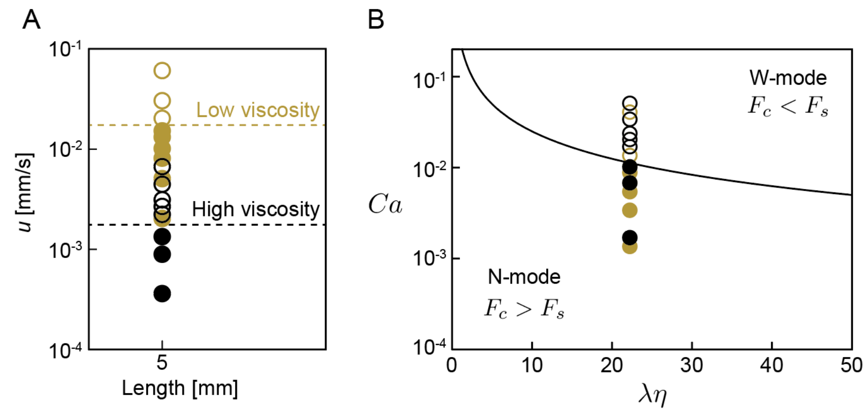

Fig. S3. Effects of liquid viscosity. (A) Experimental results of two liquids with different viscosity, but the same surface tension. As increasing the viscosity, the drain rate of the transition point decreases. **(B)** Universal regime map based on a theoretical model. Open and closed symbols indicate W-mode and N-mode, respectively.

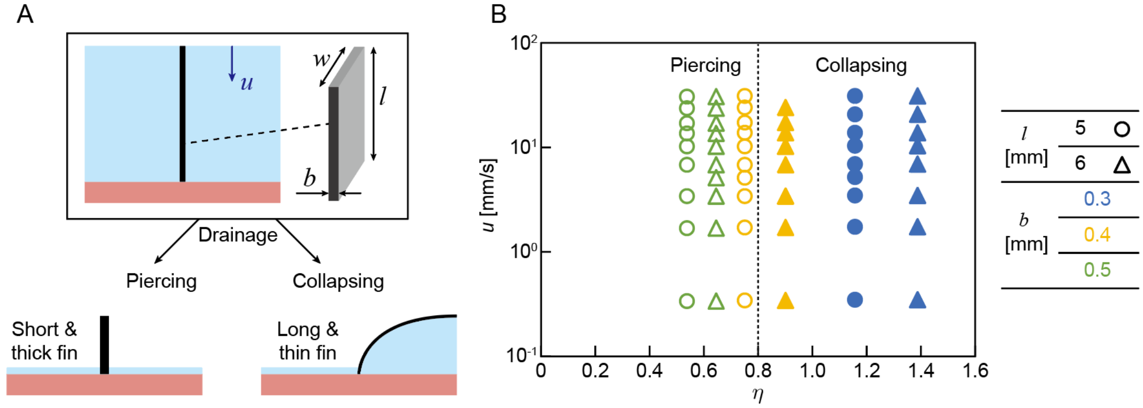

Fig. S4. Limits of fin stiffness and operation in the far-wall limit. (A) Schematics of piercing and collapsing after drainage. Thick fins pierce the liquid interface and resist buckling. Thin fins, such as those used in flap4s, collapse by bending or buckling due to capillary forces. **(B)** Theoretical regime map governed by the elastocapillary number, $\eta = l/l_{ec}$. Depending only on η, we can distinguish between the two regimes: piercing versus collapsing.

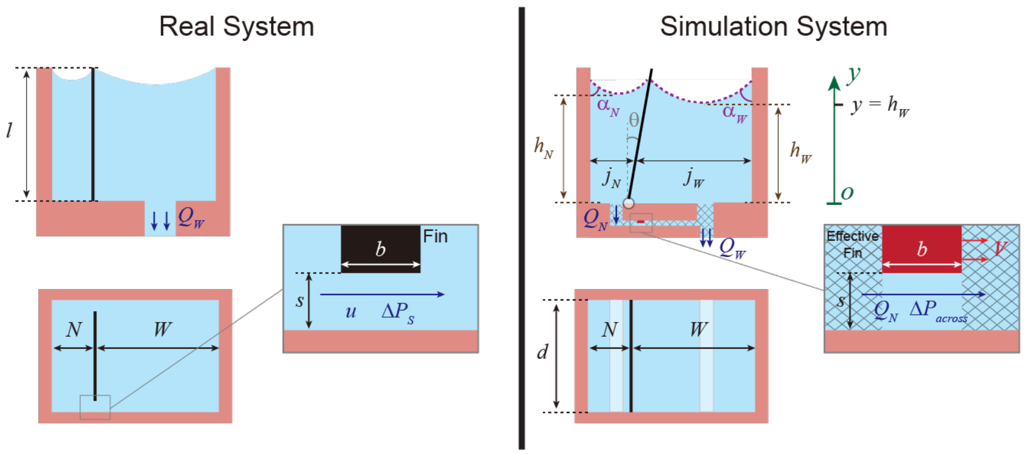

Fig. S5. Schematics of the real system (on the left) and the reduced order model system (on the right). The out-of-plane leakage through the spacing *s* in the real system is replaced with a leakage channel within the 2D reduced-order model. Only the region confined by the effective fin length *b* and the channel spacing s is the leakage channel in which leakage flow Q_N develops. The hatched blue region represents an ideal free flow area added in the reduced-order model solely to visualize the continuity of flow in the device, and hence no hydrodynamic effects are considered in the hatched region. To transfer forces from the leakage flow to the fin, a fin avatar -shown in red- slides within the channel while being connected to the center point of the fin by a rigid bar (omitted in the schematic). Namely, the fin avatar moves at the same average linear velocity *V* as the center point of the actual fin and transfers the torque to the actual fin, accounting for the leakage pressure drop and shear load in the horizontal direction.

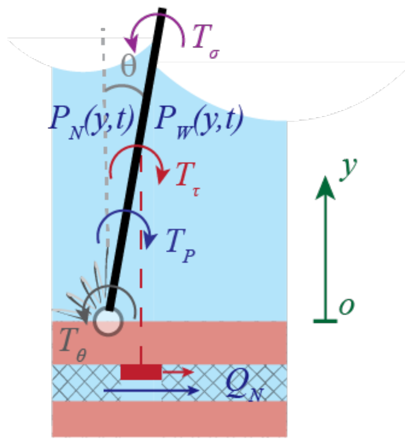

Fig. S6. Free body diagram of the fin separating the liquid on narrow/wide chamber. $P_N(y,t)$ and $P_N(y,t)$ represent the liquid pressures from the narrow and wide sides, respectively, which causes a torque T_P. The effective fin (fin avatar) is rigidly connected with the middle of the fin (red dashed line) causing the transmission of the leakage shear force to a torque $T\tau$ onto the fin. The height difference of the meniscus on each chamber exerts a torque T_σ onto the fin. The torsional spring at the pivot provides an elastic resisting torque T_θ.

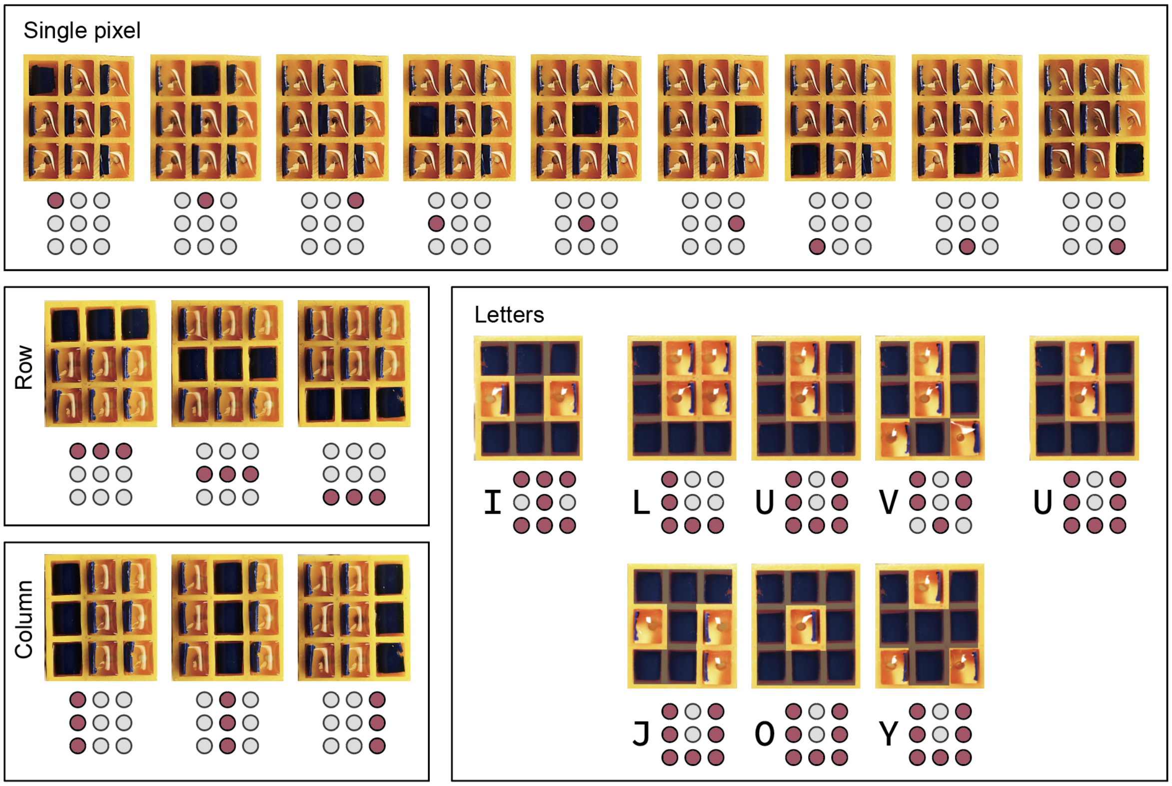

Fig. S7. Pixelated soft display devices. Simple signals in 3 × 3 panel. The width of a single pixel is 4 mm.

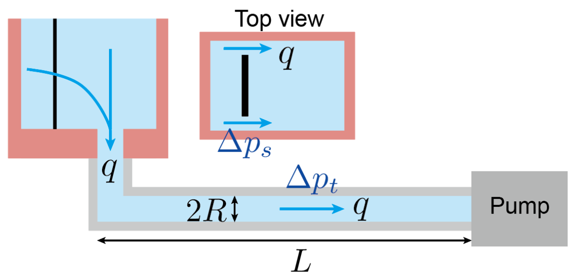

Fig. S8. Experimental setup showing the components where viscous dissipation takes place. Δp_s and Δp_t correspond to the pressure difference at the flap4 device and the tubing, respectively.

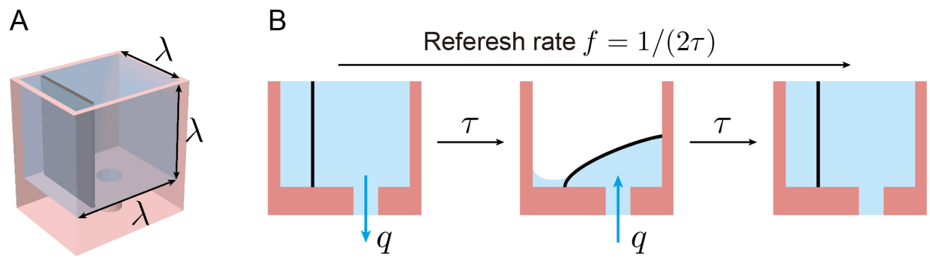

Fig. S9. Refresh rate of flap4. (A) A cubic flap4 cell in uniform pixel size λ. **(B)** The description of the refresh rate of flap4. The drainage and filling time scales are the same $\tau \sim \lambda^3/q$, where λ^3 represents the cell volume.

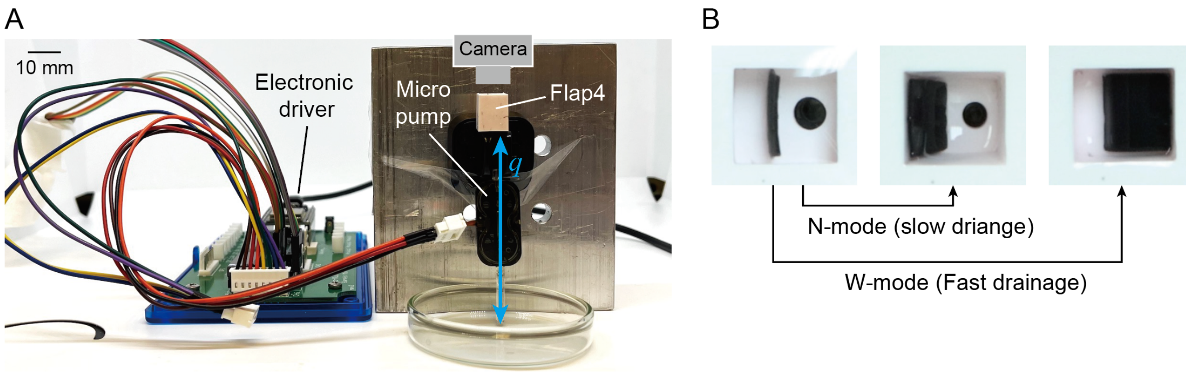

Fig. S10. Flap4 operated by piezohydraulic pump. (A) Experimental setup. The micropump supplies IPA to flap4 against gravity, while the electronic driver sends a 200 Hz signal to the micropump. **(B)** Top view images of flap4. Flap4 displays the N-mode and W-mode at slow drainage (q = 0.8 ml/min) and fast drainage (q = 6 ml/min), respectively.

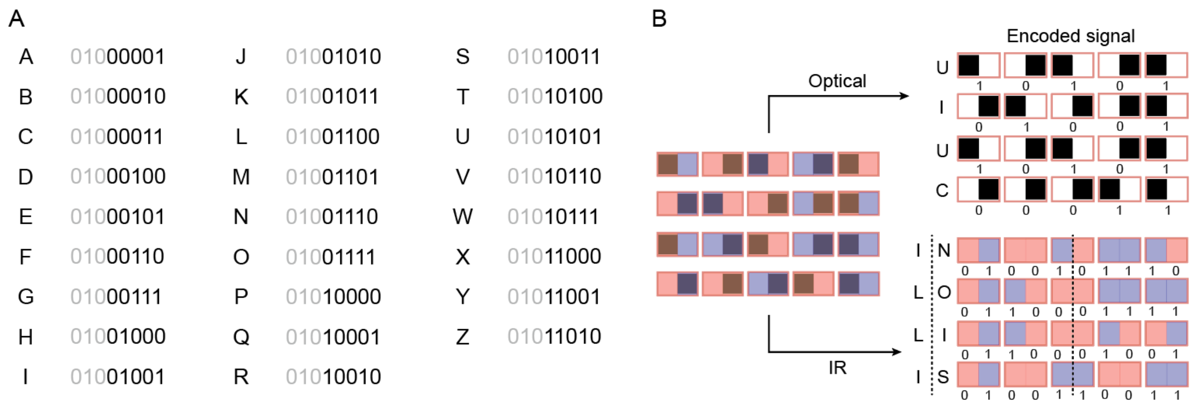

Fig. S11. Binary signal systems. (A) Code description of binary codes (ASCII). The gray colors are repetitive numbers and are not considered in this binary signal system. **(B)** The arrays of flap4s show different binary signals in optical and IR domains. One can refer to the code numbers in caption (A).

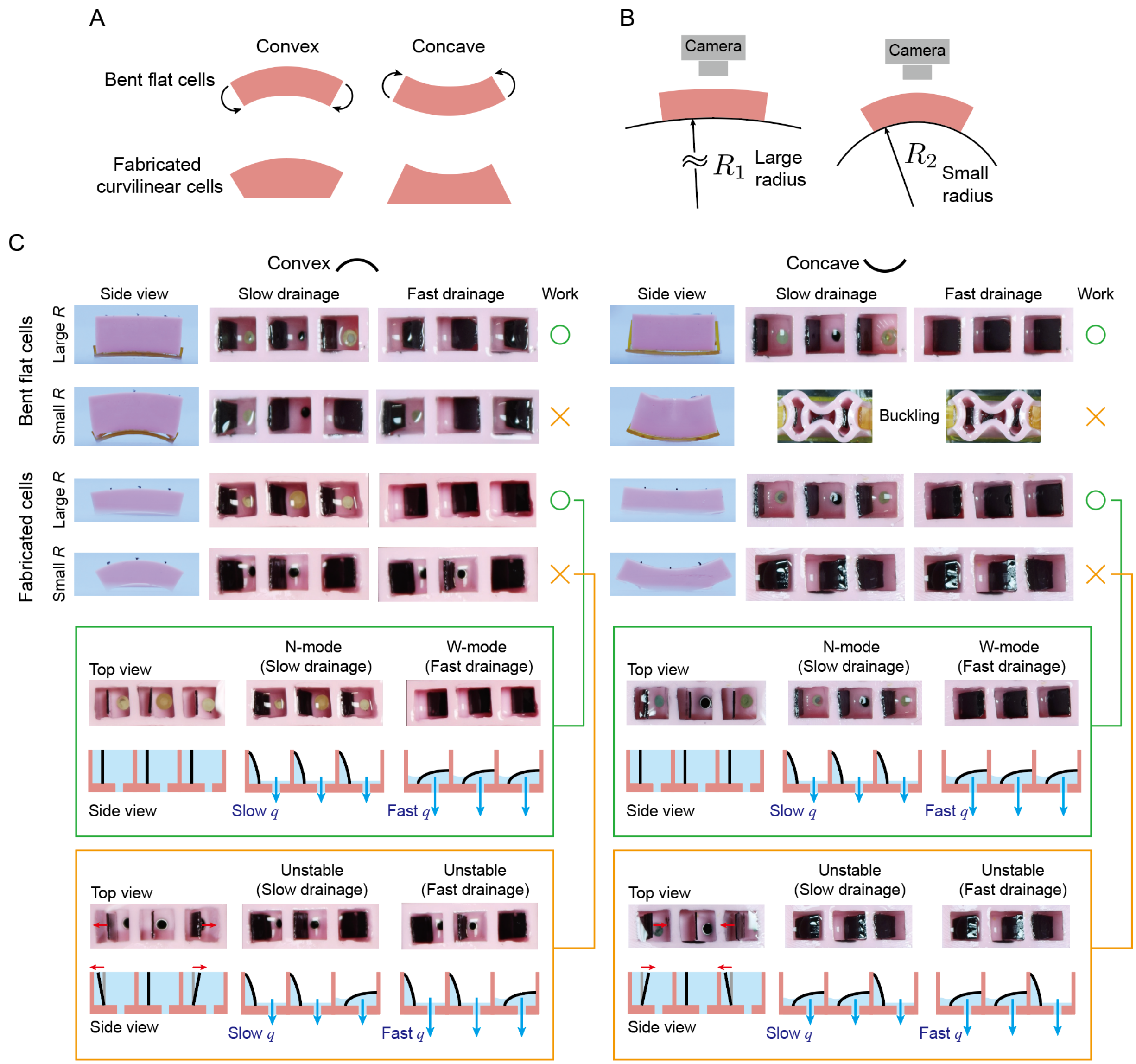

Fig. S12. Flpa4 operation test on curved surface. (A) Two types of curved surface in convex and concave shape. **(B)** Experimental setup of operation test. **(C)** Stable operation of morphing texture with various curved configuration. The left and right column correspond to convex and concave surfaces. The operation is stable when R_1 = 100 mm (green O) and unstable when R_2 = 25 mm (orange X). The red arrows represent the initial deformation of the fins due to geometrical effects. Slow and fast drain rates are q = 0.42 ml/min and 4.2 ml/min, respectively. Flat plane illustrations (side view) are used for simplicity, despite the curved nature of flap4. The working liquid is mineral oil.

Liquid	Viscosity (Pa·s)	Density (kg/m^3)	Surface tension (N/m)
Mineral oil (light)	0.02	870	0.03
Mineral oil (heavy)	0.15		

Table S1. Liquid properties

Display	Visual perception	Mechanism	Energy density [mW/cm^2]	Pixel size [mm]
Flap4	Reflection	Hydrodynamics	$\sim 10^1$	≈ 7
E-paper	Reflection	Electrophoretic	$\sim 10^2$	$\sim 10^{-1}$
LED	Illumination	Light emission	$\sim 10^0$	$\sim 10^0$
LCD	Illumination	Liquid crystal & back light	$\sim 10^1$	$\sim 10^{-2}$

Table S2. Display specification. The power consumption is measured at a refresh rate of 30 Hz (*23*, *24*).

Movie S1. Bimorphic of single fin

Movie S2. Numerical simulation of the single fin device using reduced order model

Movie S3. Polymorphic double fin

Movie S4. Polymorphic four fins (domino)

Movie S5. Bimorhic petal-shaped fins (flower)

Movie S6. Multipixel soft display devices

Movie S7. IR encoding system using temperature regulation

REFERENCES AND NOTES

1. J. Teyssier, S. V. Saenko, D. van der Marel, M. C. Milinkovitch, Photonic crystals cause active colour change in chameleons. *Nat. Commun.* **6**, 6368 (2015)

2. J. B. Messenger, Cephalopod chromatophores: Neurobiology and natural history. *Biol. Rev.* **76**, 473–528 (2001)

3. J. P. Vigneron, J. M. Pasteels, D. M. Windsor, Z. Vértesy, M. Rassart, T. Seldrum, J. Dumont, O. Deparis, V. Lousse, L. P. Biró, D. Ertz, V. Welch, Switchable reflector in the Panamanian tortoise beetle *Charidotella egregia* (Chrysomelidae: Cassidinae). *Phys. Rev. E. Stat. Nonlin. Soft Matter Phys.* **76**, 031907 (2007).

4. J. W. Weisel, C. Nagaswami, R. O. Peterson, River otter hair structure facilitates interlocking to impede penetration of water and allow trapping of air. *Can. J. Zool.* **83**, 649–655 (2005).

5. S. S. N. Gorb, *Attachment Devices of Insect Cuticle* (Kluwer, 2001)

6. R. F. Shepherd, F. Ilievski, W. Choi, S. A. Morin, A. A. Stokes, A. Mazzeo, X. Chen, M. Wang, G. M. Whitesides, Multigait soft robot. *Proc. Natl. Acad. Sci. U.S.A.* **108**, 20400–20403 (2011).

7. J. H. Pikul, S. Li, H. Bai, R. T. Hanlon, I. Cohen, R. F. Shepherd, Stretchable surfaces with programmable 3D texture morphing for synthetic camouflaging skins. *Science* **358**, 210–214 (2017).

8. E. Siéfert, E. Reyssat, J. Bico, B. Roman, Bio-inspired pneumatic shape-morphing elastomers. *Nat. Mater.* **18**, 24–28 (2019).

9. M. A. Unger, H.-P. Chou, T. Thorsen, A. Scherer, S. R. Quake, Monolithic microfabricated valves and pumps by multilayer soft lithography. *Science* **288**, 113–116 (2000).

10. M. D. Volder, D. Reynaerts, Pneumatic and hydraulic microactuators: A review. *J.*

Micromech. Microeng. **20**, 043001 (2010).

11. H.-Y. Kim, L. Mahadevan, Capillary rise between elastic sheets. *J. Fluid Mech.* **548**, 141 (2006).

12. J. Hwang, J. Ha, R. Siu, Y. S. Kim, S. Tawfick, Swelling, softening, and elastocapillary adhesion of cooked pasta. *Phys. Fluids* **34**, 042105 (2022)

13. J. Ha, Y. S. Kim, K. Jiang, R. Siu, S. Tawfick, Hydrodynamic elastocapillary morphing of hair bundles. *Phys. Rev. Lett.* **125**, 254503 (2020).

14. J. Ha, Y. S. Kim, R. Siu, S. Tawfick, Dynamic pattern selection in polymorphic elastocapillarity. *Soft Matter* **18**, 262–271 (2022)

15. A. Hadjittofis, J. R. Lister, K. Singh, D. Vella, Evaporation effects in elastocapillary aggregation. *J. Fluid Mech.* **792**, 168–185 (2016)

16. C. C. Chiao, J. K. Wickiser, J. J. Allen, B. Genter, R. T. Hanlon, Hyperspectral imaging of cuttlefish camouflage indicates good color match in the eyes of fish predators. *Proc. Natl. Acad. Sci. U.S.A.* **108**, 9148–9153 (2011).

17. D. J. Kemp, M. F. Herberstein, L. J. Fleishman, J. A. Endler, A. T. Bennett, A. G. Dyer, N. S. Hart, J. Marshall, M. J. Whiting, An integrative framework for the appraisal of coloration in nature. *Am. Nat.* **185**, 705–724 (2015).

18. P. Rothemund, A. Ainla, L. Belding, D. J. Preston, S. Kurihara, Z. Suo, G. M. Whitesides, A soft, bistable valve for autonomous control of soft actuators. *Sci. Robot.* **3**, eaar7986 (2018).

19. T. Chen, M. Pauly, P. M. Reis, A reprogrammable mechanical metamaterial with stable memory. *Nature* **589**, 386–390 (2021).

20. D. Rus, M. T. Tolley, Design, fabrication and control of soft robots. *Nature* **521**, 467–475 (2015).

21. C. Hu, S. Pané, B. J. Nelson, Soft micro- and nanorobotics. *Annu. Rev. Control Robot. Auton. Syst.* **1**, 53–75 (2018).

22. P. Grandgeorge, N. Krins, A. Hourlier-Fargette, C. Laberty-Robert, S. Neukirch, A. Antkowiak, Capillarity-induced folds fuel extreme shape changes in thin wicked membranes. *Science* **360**, 296–299 (2018).

23. J. Heikenfeld, P. Drzaic, J. S. Yeo, T. Koch, Review paper: A critical review of the present and future prospects for electronic paper. *J. Soc. Inf. Disp.* **19**, 129–156 (2011).

24. M. R. Fernández, E. Z. Casanova, I. G. Alonso, Review of display technologies focusing on power consumption. *Sustainability* **7**, 10854–10875 (2015).

25. W. E. Wilson, *Positive Displacement Pumps and Fluid Motors* (Pitmann Pub. Co. Corp. 1950).

26. L. D. Mauck, C. S. Lynch, Piezoelectric hydraulic pump development. *J. Intell. Mater. Syst. Struct.* **11**, 758–764. (2000).